Model Predictive Pulse Pattern Control for the Five-Level Active Neutral Point Clamped Inverter

Nikolaos Oikonomou, *Member, IEEE*, Christof Gutscher, Petros Karamanakos, *Student Member, IEEE*, Frederick Kieferndorf, *Member, IEEE*, and Tobias Geyer, *Senior Member, IEEE*

Abstract—In this paper, the recently introduced control strategy referred to as model predictive pulse pattern control (MP³C) is adapted to the ACS 2000 five-level power converter of ABB. The drive consists of an induction machine and a five-level active neutral-point clamped (ANPC-5L) inverter. The power inverter is fed with optimized pulse patterns (OPPs) that produce minimum harmonic distortion in the stator winding of the ac machine. An optimal stator flux trajectory is calculated from these OPPs and a trajectory controller tracks it in real-time. In the proposed approach, trajectory tracking is based on model predictive control (MPC): a constrained optimal control problem is formulated and solved in real-time in a time-efficient manner. An event-based prediction horizon is employed in order to ensure fast tracking of the stator flux trajectory. The advantages of the proposed method are optimal steady-state behavior in terms of harmonic distortion and fast torque response. The method was tested on a pilot ACS 2000 power converter coupled to a general-purpose 1.21-MW induction machine. Experimental results were obtained from this industrial setup; they are presented in this paper to demonstrate the high performance of MP³C.

Index Terms—AC drive, optimized pulse pattern, model predictive control, five-level active neutral point inverter

I. Introduction

ABB has recently introduced the ACS 2000 general-purpose medium-voltage (MV) drive to provide speed and torque control in a wide range of applications that include control of industrial fans and pumps [1]. Fig. 1 shows the circuit diagram of the drive configuration that includes the active rectifier stage, the dc link, and the power inverter stage that controls a MV induction machine. The ACS 2000 is based on the five-level active neutral-pointed clamped (ANPC-5L) topology [2]; the circuit diagram of one phase leg of the ANPC-5L topology is shown in Fig. 2.

General-purpose drives can be used to control standard direct-on-line (DOL) induction machines, which are characterized by a low value of leakage inductance x_σ, usually in the range of 0.18 p.u.. In the inverter-controlled configuration of Fig. 1, a DOL machine is fed with pulse width modulated (PWM) voltage waveforms. The minimization of the harmonic distortion of the stator currents is of special interest; this is a particularly challenging task owing to the low value of x_σ.

Increasing the switching frequency of the semiconductor switches would allow minimizing the distortion of the output voltage waveforms and of the machine currents. However, the switching frequency cannot be increased beyond a few hundred Hertz per semiconductor in MV configurations such as that of the ACS 2000 because of thermal constraints imposed by the IGBT technology of the semiconductor devices. A further limiting factor is the number of additional switching transitions that are required to control the neutral point potential and the voltage of the phase capacitors of ACS 2000 around their reference values. The neutral point N of the shared dc-link and the phase capacitor C_{ph} of one phase leg of the ANPC-5L are shown in Fig. 2. Waveforms of the neutral point potential and of the three-phase phase capacitor voltages are shown at steady-state operation in Fig. 3. The additional pulses that are necessary to control the neutral point potential and the phase capacitor voltages make use of the inherent voltage redundancies of ANPC-5L; the method for establishing control of the converter-internal voltages is presented in [3].

The choice of the PWM method is crucial to reduce the harmonic distortion without violating the limitation in the switching frequency. Conventional PWM methods, such as carrier-based PWM and space vector modulation (SVM), can achieve this result only in a limited range of the modulation area, typically below 50% of the rated voltage of the power converter [4].

A more suitable solution is offered through the use of synchronous optimal modulation: offline-calculated optimal pulse patterns (OPPs) [5]–[7] can achieve values of the total demand distortion (TDD) of the machine current lower than 5% of the rated current in the complete linear range of the modulation index m. Individual current harmonics of non-triplen order (5th, 7th, 11th, 13th, ...) are reduced and interharmonic components are eliminated [4].

However, the use of OPPs in a closed-loop control system is difficult in practice: discontinuities of the switching angles and
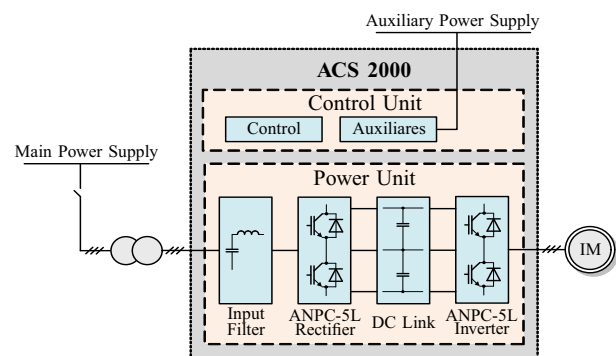
N. Oikonomou, F. Kieferndorf, and T. Geyer are with ABB Corporate Research, Baden-Dättwil, Switzerland; e-mails: nikolaos.oikonomou@ch.abb.com, frederick.kieferndorf@ch.abb.com, and t.geyer@ieee.org

C. Gutscher is with ABB Switzerland LTD., Medium Voltage Drives, Turgi, Switzerland; e-mail: christof.gutscher@ch.abb.com

P. Karamanakos is with the Department of Electrical and Computer Engineering, National Technical University of Athens, Athens, Greece; e-mail: petkar@central.ntua.gr
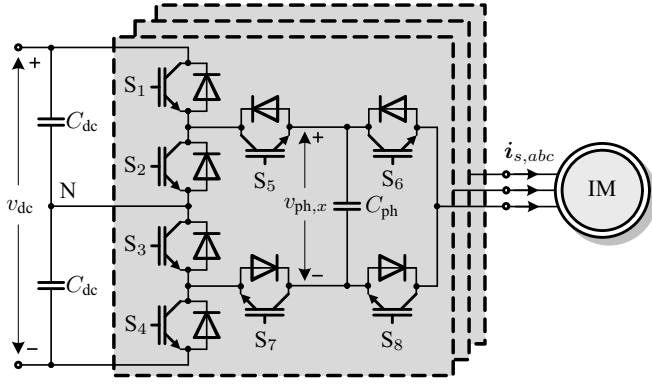
Fig. 1: The ACS 2000 from ABB: Drive configuration.

Fig. 2: Circuit diagram of the five-level active neutral point clamped (ANPC) voltage source inverter driving an induction machine (IM).
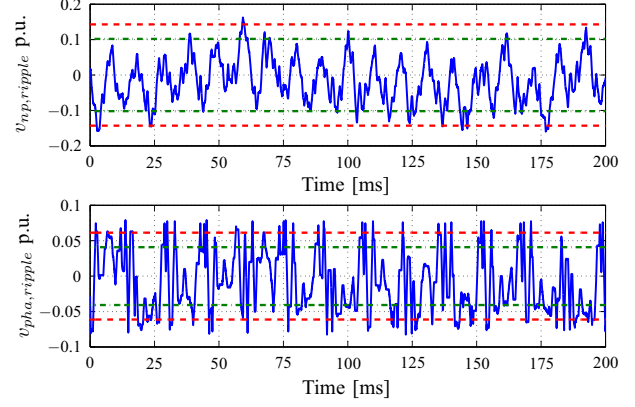

Fig. 3: Converter-internal voltage waveforms of the ACS 2000 recorded at 32 Hz and 42% load; *Top*: neutral point potential, *Bottom*: ac ripple of phase capacitor voltage. Both values are shown in p.u..

transitions between neighboring pulse patterns can introduce harmonic excursions [4]. Fig. 4(c) shows the switching angles of OPPs of pulse number $d = 5$ per quarter wave plotted over the modulation index; a high number of discontinuities in the switching angles can be observed. A solution is offered through control by trajectory tracking [4]. It allows maintaining the optimal volt-seconds balance of OPPs under quasi steady-state conditions, even when the pulse number d changes. Establishing control by trajectory tracking of the stator flux trajectory is a preferred method since it does not require estimating the leakage inductance of the machine in real-time [4]. However, state-of-the art flux trajectory tracking requires real-time estimation of the fundamental of the stator flux trajectory *separately* from the flux harmonics [8].

A more recent solution that addresses this problem is model predictive pulse pattern control (MP³C) [9]. The stator flux control problem is addressed from the perspective of model predictive control (MPC) [10], [11]. Based on a mathematical model of the system an objective function is formulated; this function is minimized by correcting the deviation from an optimal flux trajectory within a time prediction horizon of finite length. The present paper is an *industrial* implementation of MP³C, tailored to the requirements of the ACS 2000: the underlying optimization problem is solved in real-line in a time-efficient manner to provide the sequence of switching angles (the control input) that allows operation with OPPs at quasi steady-state. The deadbeat implementation of MP³C in [9] is refined to achieve high dynamic performance in closed

loop despite of computational limitations in the length of the prediction horizon.

II. PRINCIPLE OF STATOR FLUX TRAJECTORY TRACKING

Optimized pulse patterns are calculated offline and stored in a look-up table for use in real-time operation, [5]–[7]. The entries of the look-up table are read out in real-time by making use of the modulation index m and the pulse number d as inputs as shown in the block diagram of Fig. 5. The pulse number d is selected depending on the fundamental frequency of the drive system f_1 as $d = floor(f_{sw}/f_1)$, where f_{sw} is the switching frequency of the semiconductor devices. The selection $f_{sw} = f_{sw,max}$ ensures that the maximum value of the switching frequency is not exceeded. The modulation index m is adjusted through a conventional linear controller of the rotor flux amplitude ψ_r of the ac machine, Fig. 5.

The pair (m, d) defines the operating point of the drive system through the optimized pulse sequence $\boldsymbol{P}(m, d)$, Fig. 5. An example of an optimized three-phase pattern which is valid for $m = 0.55$ and $d = 5$ is shown in Fig. 4(b). When fed to the electrical machine through the power converter without further modification, the optimized pulse pattern generates three-phase voltages in the stator windings whose sinusoidal spatial distributions are described by the respective voltage space vector $\boldsymbol{u}_s$, shown in the vector diagram of Fig. 6. The

(a) Optimized pulse pattern; $d = 5$, $m = 0.55$, phase a.

(b) Three-phase optimized pulse pattern; $d = 5$, $m = 0.55$.
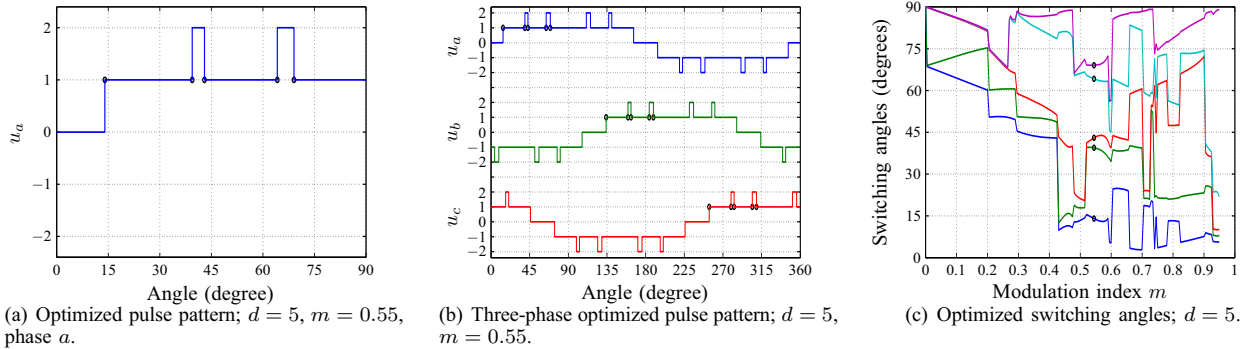
(c) Optimized switching angles; $d = 5$.

Fig. 4: Five-level optimized pulse pattern with $d = 5$ switching angles per quarter wave. The switching angles at $m = 0.55$ are indicated by black circles.
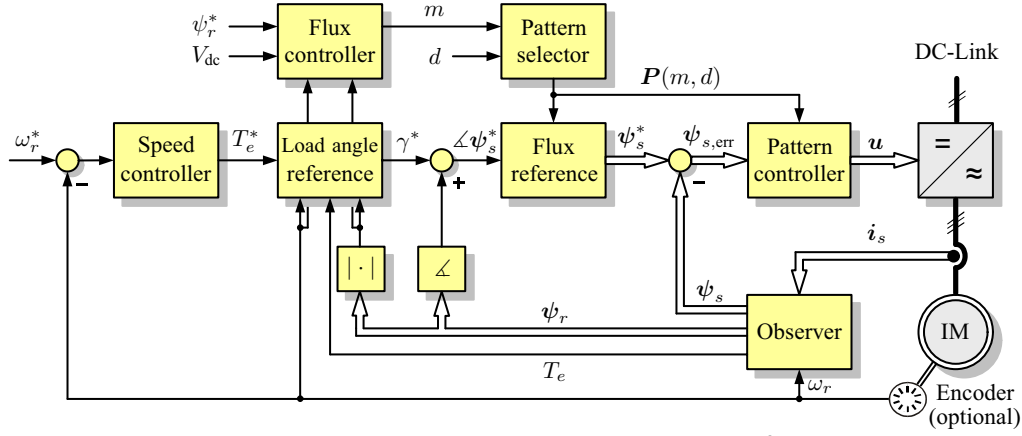
Fig. 5: Block diagram of the model predictive pulse pattern control (MP³C) method.
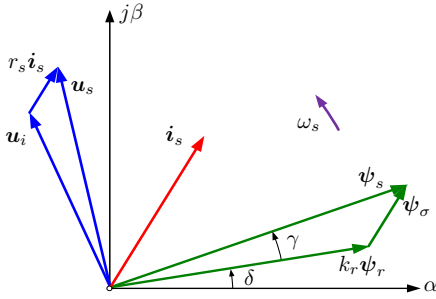

Fig. 6: Diagram of voltage, current, and flux linkage space vectors in an induction motor.

electromagnetic field in the stator winding is described by the stator flux space vector

$$\boldsymbol{\psi}_s(t) = \boldsymbol{\psi}_s(0) + \int_0^t \boldsymbol{u}_s(\tau)d\tau \,, \qquad (1)$$

also shown in Fig. 6. Assuming operation at steady-state and a power converter of ideal switching behavior, the stator flux space vector would track an optimized reference flux trajectory; an example is shown in Fig. 7(a) over one quarter of the fundamental period. Under ideal conditions, the voltage in the stator windings would match exactly the optimized pulse pattern waveforms and the harmonic distortion of the stator currents would be equal to its offline-calculated value.

However, the behavior of the drive system is non-ideal owing to non-linear effects of the power converter. These include instantaneous deviations of the neutral point potential from zero, deviations of the phase capacitor voltages from their reference values, and non-idealities of the power converter system such as the dead-time effect [12]. The instantaneous excursions of the converter-internal voltage waveforms shown in Fig. 3 from their reference values are manifested as deviations of the flux space vector from its reference trajectory. The result is increased harmonic content in the stator currents of the machine despite the utilization of optimized pulse patterns. In addition to this, deviations from the reference flux trajectory occur when the drive operates dynamically, e.g. at step changes of the load torque or at the event of a ride-through condition. Such errors have to be compensated very quickly to avoid a trip due to overcurrent conditions in the drive system.

Any deviation of the stator flux space vector $\boldsymbol{\psi}_s$ from its reference trajectory $\boldsymbol{\psi}_s^*$ can be described by the flux error space vector

$$\boldsymbol{\psi}_{s,\mathrm{err}} = \boldsymbol{\psi}_s^* - \boldsymbol{\psi}_s \,. \qquad (2)$$

Control by stator flux trajectory tracking aims at compensating the stator flux error $\boldsymbol{\psi}_{s,\mathrm{err}}$ in real-time by modifying the volt-second area of the original, offline-calculate pulse pattern $\boldsymbol{P}(m, d)$, which is valid only for an ideal system operated at steady-state, [4]. Eliminating the flux error allows the drive system to perpetuate the operating point (m, d) while generating currents of minimum harmonic distortion in the stator windings of the machine. This is due to the linear relationship between flux and current harmonics: optimization of the stator flux trajectory amounts to optimal current waveforms in the machine windings [4].

Moreover, stator flux trajectory tracking also enables torque control. This is explained with reference to the vector diagram in Fig. 6 that shows the space vector of the stator- and rotor flux linkage, which describe the electrical subsystem of the ac machine [13]. For reasons of completeness, Fig. 6 shows the space vectors of further electrical quantities of the ac machine at motoring operation: the flux leakage is the difference between stator- and rotor flux, $\boldsymbol{\psi}_\sigma = \boldsymbol{\psi}_s - k_r \boldsymbol{\psi}_r$; the stator voltage is the sum of the induced voltage and the voltage drop on the stator resistance, $\boldsymbol{u}_s = \boldsymbol{u}_i + r_s \boldsymbol{i}_s$, where $\boldsymbol{i}_s$ is the stator current. The amplitude of the flux vectors and their angular displacement γ determine the amount of torque T_e generated at the rotor shaft of the machine by the interaction of the electromagnetic field of the stator- and rotor windings through the air gap,

$$T_e = k_r \psi_r \psi_s \sin\gamma \,, \qquad (3)$$

where k_r is the rotor coupling factor. Assuming knowledge of the quantities in (3) and a given reference torque value T_e^*, the problem of torque control converts into adjusting the stator flux space vector $\boldsymbol{\psi}_s$ to coincide in intensity and angular displacement with the reference flux $\boldsymbol{\psi}_s^*$ at any given time instant t.

The procedure is explained with reference to the block diagram in Fig. 5, where the torque reference T_e^* is the output of a conventional speed controller. An observer of the
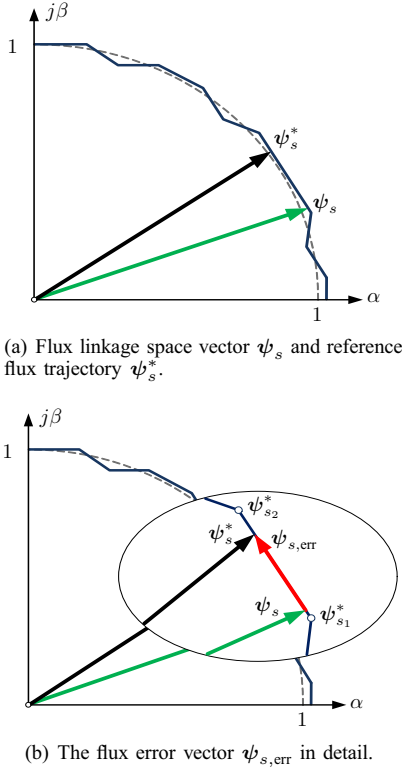
131

(a) Flux linkage space vector $\boldsymbol{\psi}_s$ and reference flux trajectory $\boldsymbol{\psi}_s^*$.

(b) The flux error vector $\boldsymbol{\psi}_{s,\text{err}}$ in detail.

Fig. 7: The reference flux vector $\boldsymbol{\psi}_s^*$ is calculated in real-time by linear interpolation between the pre-stored values $\boldsymbol{\psi}_{s_1}^*$ and $\boldsymbol{\psi}_{s_2}^*$.

state variables that describe the electrical machine is fed by the measured stator current $\boldsymbol{i}_s$ and the angular velocity of the rotor ω_r [14]. The observer estimates the complex state variables $\boldsymbol{\psi}_s$ and $\boldsymbol{\psi}_r$, and the electromagnetic torque (3). The amplitude of the rotor flux space vector $\boldsymbol{\psi}_r$ is controlled to be constant in the base speed range, as shown in Fig. 5. Its angular displacement δ with reference to the real axis of the stationary coordinate system (Fig. 6) is estimated in real time as $\delta = arg(\boldsymbol{\psi}_r)$.

With the actual state of the electrical machine estimated by the observer, the next task is to retrieve the phase angle of the the the reference flux $\boldsymbol{\psi}_s^*$ that corresponds to the reference torque value T_e^*. When the machine is fully magnetized, the magnitude of the reference flux vector is equal to 1 p.u.. Then, for a constant value of the rotor flux magnitude and a given torque reference, the desired angle between the stator and rotor flux vectors is calculated,

$$\gamma^* = \sin^{-1}\left(\frac{T_e^*}{k_r \psi_r \psi_s^*}\right). \qquad (4)$$

The reference flux vector is then obtained by integrating the chosen three-phase pulse pattern; the reference angle $\gamma^* + \delta$ is the upper limit of the integral in (1). With this procedure, the torque- and the flux control problem of the drive system can be resolved now by compensating the error vector $\boldsymbol{\psi}_{s,\text{err}}$. The details of the implementation of trajectory tracking for the specific case of the ACS 2000 drive system are explained in the following Section.

III. MODEL PREDICTIVE PULSE PATTERN CONTROL (MP^{3}C) FOR ACS 2000

The control objective of the proposed method is to compensate the flux error in real-time by modifying the pre-calculated switching instants of the OPPs. The flux error compensation has to be achieved as fast as possible, and by delivering low distortion in the machine currents in the complete modulation index range. In a first step, the reference flux trajectory is calculated offline by integrating the respective OPPs over a complete period of the fundamental voltage waveform. The result of the integration procedure is stored in a look-up table. Thus, the following information is readily available at each operating point of the discretized modulation range:

i) the switching angles of the OPPs; owing to the quarter-wave symmetry of the optimized pulse sequences, Fig. 4, only the angles over the first 90° of the fundamental period need to be stored in the look-up table,

ii) the respective switching states over 90° of the fundamental voltage space vector, and

iii) the component values $\psi_{s,\alpha}^*$ and $\psi_{s,\beta}^*$ of the reference flux vector referred to in stationary coordinates, i.e. $\boldsymbol{\psi}_s^* = \psi_{s,\alpha}^* + j\psi_{s,\beta}^*$. The reference flux trajectory is 30°-symmetric, Fig. 7. Thus, only the value pairs $(\psi_{s,\alpha}^*, \psi_{s,\beta}^*)$ are stored in the look-up table.

Storing the reference flux coordinates in the look-up table – rather than calculating them in real-time through (1) – reduces greatly the complexity of mathematical operations that need to be performed in real-time.

Two steps are needed to calculate the actual value of the reference vector $\boldsymbol{\psi}_s^*$. First, the components of the reference flux vectors $\boldsymbol{\psi}_{s_1}^*$ and $\boldsymbol{\psi}_{s_2}^*$ that are adjacent to the reference flux vector are retrieved from the look-up table. The calculation of the angular position of the reference flux vector $\angle \boldsymbol{\psi}_s^*$ is required to achieve this; the procedure was described in Section II. In a second step, the reference vector is calculated by performing linear interpolation between $\boldsymbol{\psi}_{s_1}^*$ and $\boldsymbol{\psi}_{s_2}^*$ (see Fig. 7), a process that requires very few mathematical calculations.

The correction of the flux error $\boldsymbol{\psi}_{s,\text{err}}$ is achieved by modifying in real-time the pre-stored switching instants of the OPPs. The volt-second area that the PWM sequence of each phase contributes is either increased or decreased depending on the direction of the modification and of the switching transition. An example is shown in Fig. 8(a), where the volt-second area of the pulse in phase a is reduced by Δt_a. Furthermore, a modification of the switching instant $t_{b_1}^*$ is made in phase b of Fig. 8(a): the volt-second area is increased by Δt_b in this case. Both modifications Δt_a and Δt_b are made such that the respective a- and b-components of a stator flux error $\boldsymbol{\psi}_{s,\text{err}}$ are minimized. In general, modifying the value of a pre-calculated (nominal) switching instant t_x^*, $x \in \{a, b, c\}$, by a time interval Δt_x results in a modified switching instant $t_x = t_x^* + \Delta t_x$. The volt-second contribution of phase x to the flux correction is:

$$\Delta \boldsymbol{\psi}_{s,x}(\Delta t_x) = -\frac{V_{\text{dc}}}{2}\Delta u_x \Delta t_x, \qquad (5)$$

where $\Delta u_x \in \{-1, +1\}$ is the direction of the switching transition and V_{dc} is the total voltage across the two dc-link
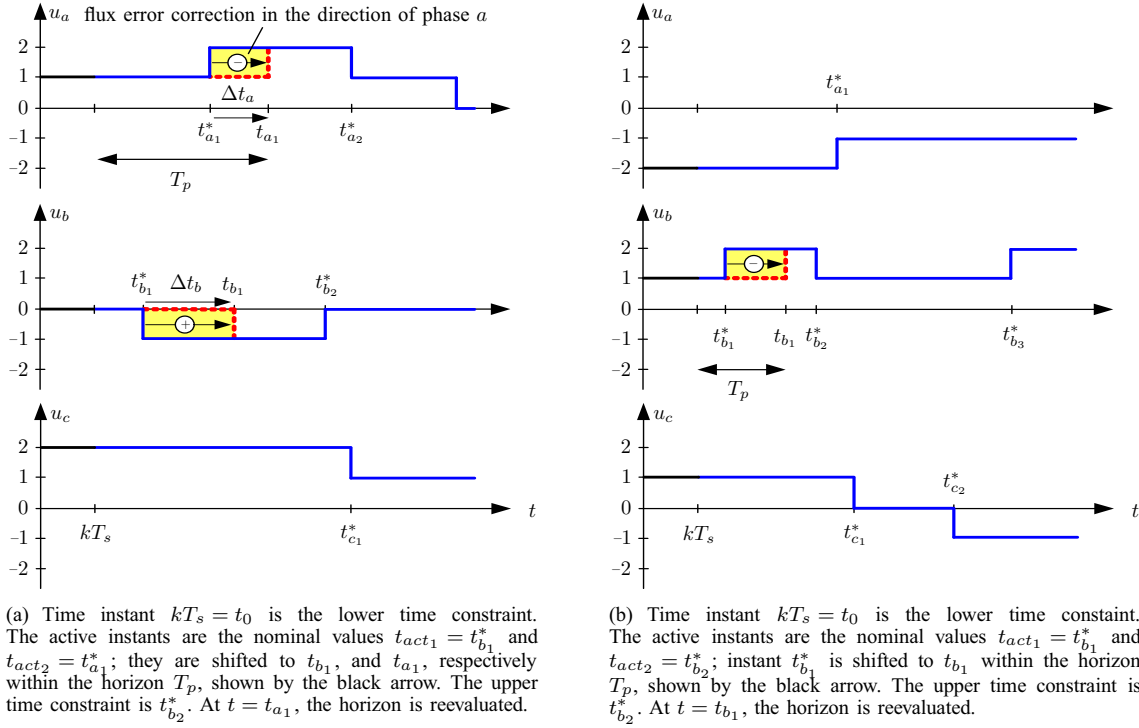
132

(a) Time instant $kT_s = t_0$ is the lower time constraint. The active instants are the nominal values $t_{act_1} = t_{b_1}^*$ and $t_{act_2} = t_{a_1}^*$; they are shifted to t_{b_1}, and t_{a_1}, respectively within the horizon T_p, shown by the black arrow. The upper time constraint is $t_{b_2}^*$. At $t = t_{a_1}$, the horizon is reevaluated.

(b) Time instant $kT_s = t_0$ is the lower time constaint. The active instants are the nominal values $t_{act_1} = t_{b_1}^*$ and $t_{act_2} = t_{b_2}^*$; instant $t_{b_2}^*$ is shifted to t_{b_1} within the horizon T_p, shown by the black arrow. The upper time constraint is $t_{b_2}^*$. At $t = t_{b_1}$, the horizon is reevaluated.

Fig. 8: MP^{3}C is activated at time instant kT_s and it modifies pre-calculated switching instants of a three-phase, five-level pulse pattern.

capacitors C_{dc}.

In a next step, an objective function is formulated and it is minimized in real-time. The chosen function is:

$$J(\Delta t) = |\boldsymbol{\psi}_{s,\text{corr}}(\Delta t) - \boldsymbol{\psi}_{s,\text{err}}|, \qquad (6)$$

where $\psi_{s,\text{corr}}(\Delta t)$ is the correction of the stator flux, and $\Delta t = [\Delta t_{a_1} \ \Delta t_{a_2} \ldots \Delta t_{b_1} \ldots \Delta t_{c_1} \ldots]^T$ is the vector of the switching instant modifications, i.e. the manipulated variables. Function (6) is penalized over a prediction horizon of finite length T_p. By modifying the switching instants of the OPP within this horizon, the flux error is minimized and – if possible – eliminated. The length of the prediction horizon is not fixed: it is rather a function of the nominal switching instants and of the modified instants of the phases that switch within the horizon. The calculation of the prediction horizon T_p is outlined in the following.

Starting from the actual sampling instant $t_0 = kT_s$, two nominal switching instants t_{act_1} and t_{act_2} are identified which are closest to t_0. The following two cases are considered:

- If the two switching instants that follow t_0 occur in different phases, the flux error vector is projected onto these two phases. In this case, two active phases, i.e. two degrees of freedom, are available to compensate the error: $\{a, b\}$, $\{b, c\}$ or $\{c, a\}$. In Fig. 8(a), the two active switching instants $t_{act_1} = t_{b_1}^*$ and $t_{act_2} = t_{a_1}^*$ are in phases b and a, respectively.
- If both switching instants t_{act_1} and t_{act_2} that follow t_0 occur in the same phase, then switching instants in a single active phase, a, b or c, are available to reduce the flux error. In Fig. 8(b), both active switching instants $t_{act_1} = t_{b_1}^*$ and $t_{act_2} = t_{b_2}^*$ are in phase b.

The length of the horizon is equal to the maximum difference between the nominal and modified instants and the initial instant t_0 (Fig. 8), i.e.

$$T_p = \max \{t_x^* - t_0, t_x - t_0\}. \qquad (7)$$

Based on (7) an *event*-based horizon is defined. The selection of the prediction horizon is key to the application-oriented implementation of MP^{3}C that is outlined here. By restricting the length of the horizon to include two switching events, the computational effort is reduced: a standard microprocessor or field-programmable gate array (FPGA) device can be used to implement MP^{3}C. In practice, the time horizon is separated into equal sampling intervals of fixed length $T_s = 25\,\mu\text{s}$. MP^{3}C is executed within this sampling interval. In every iteration the horizon reduces by T_s. When the entire horizon has been scanned, a new prediction horizon T_p is evaluated according to (7) and the flux error correction procedure is repeated. A further practical issue that determines the length of the prediction horizon is associated to the interaction of the controlling microprocessor or FPGA with an external Flash hardware device, where all the offline calculated data are stored. These data, i.e. switching instants, values of switching states and reference flux coordinates, must be read out from the Flash memory at every sampling interval T_s. The interaction takes place within a fraction of the sampling interval, $T_{int} \ll T_s$. This imposes a restriction to the length of the prediction horizon T_p.

Before the optimization problem is formulated, upper and lower time constraints must be imposed on the allowed time modification of switching instants. The lower time constraint is equal to the starting time instant t_0, while the upper time
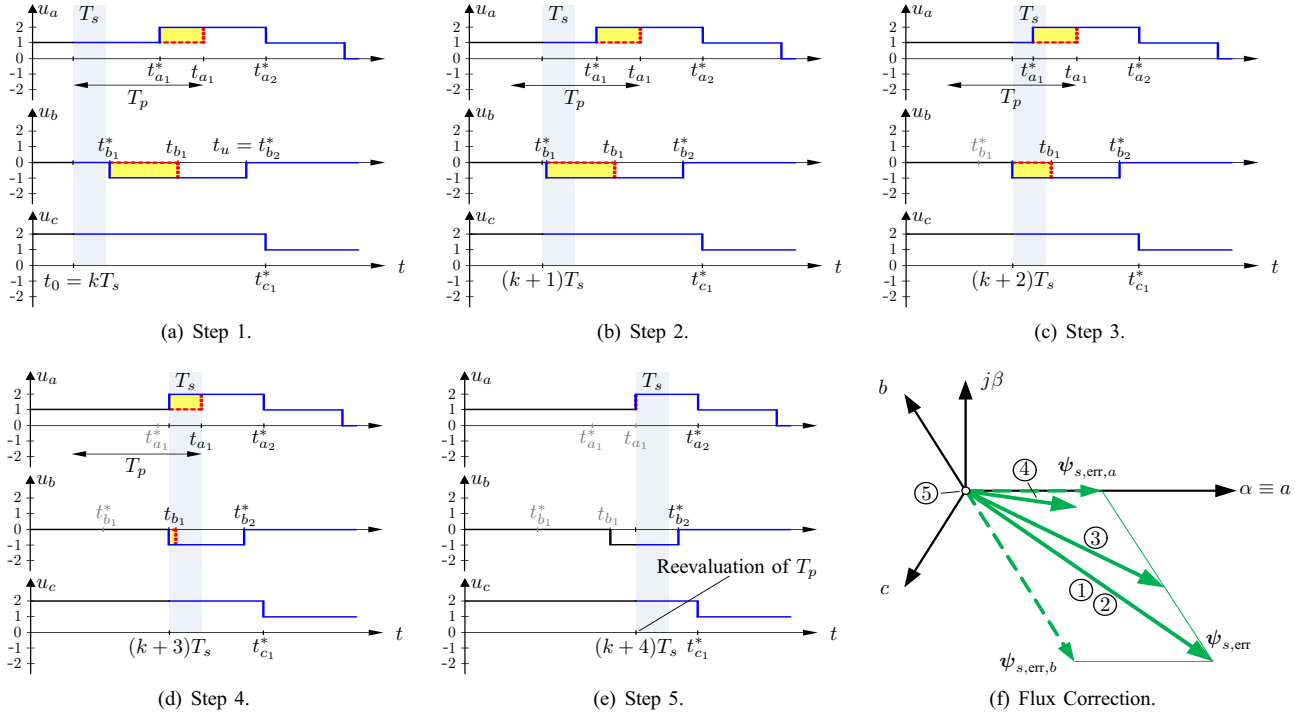
133

Fig. 9: Example of MP^{3}C compensating flux error $\psi_{s,\mathrm{err}}$ within four sampling intervals $4T_s$. The circled numbers of (f) correspond to the flux error compensation procedure shown in (a)–(e).

constraint depends on the location of the nominal values of the active switching instants. To be more specific:

- If the active switching instants t_{act_1} and t_{act_2} occur in different phases, e.g. Fig. 8(a), then the upper time constraint is equal to the nominal (pre-calculated) switching instant that first follows t_{act_1} and t_{act_2}. In the case of Fig. 8(a), where the active switching instants are $t_{act_1} = t_{b_1}^*$ and $t_{act_2} = t_{a_1}^*$, the upper time constraint is the instant $t_{b_2}^*$.
- If both active switching instants t_{act_1} and t_{act_2} occur in the same phase, e.g. Fig. 8(b), then the upper time constraint is equal to the nominal (pre-calculated) switching instant t_{act_2}. In the case of Fig. 8(b), where the active switching instants are $t_{act_1} = t_{b_1}^*$ and $t_{act_2} = t_{b_2}^*$, the upper time constraint is equal to the instant $t_{b_2}^*$.

To generalize, the time constraints are calculated as

$$t_0 \leq t_x \leq \min \{ \mathcal{T}_1 \cup \mathcal{T}_2 \} . \tag{8}$$

In (8) the set $\mathcal{T}_1$ is defined as $\mathcal{T}_1 = \{ t_x^* \,|\, t_x^* = t_{x_2}^* \}$, where $t_{x_2}^*$ is the second switching instant of the active phase/s that follow t_0, and the set $\mathcal{T}_2$ is defined as $\mathcal{T}_2 = \{ t_x^* \,|\, t_x^* = \bar{t}_{x_1}^* \}$, where $\bar{t}_{x_1}^*$ is the first switching instant of the non-active phase/s.

By taking into account the objective function, the prediction horizon T_p, and the linear time constraints given by (6), (7), and (8) respectively, the following problem is formulated:

$$\begin{aligned} &\text{minimize } J(\Delta t)\\ &\text{subject to eq. (8)} . \end{aligned} \tag{9}$$

This optimization problem is solved within every sampling interval yielding a sequence of optimal control inputs over the horizon. To solve (9), the flux error vector is projected onto

the active phases and the corresponding flux error components are calculated. The component of the flux error on each of the active phases determines the necessary modification of the nominal switching instants of the corresponding phases, (5). The modified switching instants are the optimal control inputs over the horizon. The first control input of this sequence is applied at the end of the first sampling interval; then, the length of the horizon is decreased by T_s, and the procedure is repeated. When the whole horizon has been scanned, the length of the new prediction horizon T_p is reevaluated together with the new upper and lower constraints, as described above.

Fig. 9 shows a step-by-step example of the flux error correction. The goal is to compensate the flux error $\psi_{s,\mathrm{err}}$ shown in solid line in Fig. 9(f). In Fig. 9(a), the length of the prediction horizon T_p and the lower and upper time constraints, $t_0 = kT_s$ and $t_u = t_{b_2}^*$, respectively, are determined. Also the required time modifications $\Delta t_a = -(t_{a_1}^* - t_{a_1})$ and $\Delta t_b = -(t_{b_1}^* - t_{b_1})$ are calculated within the first sampling interval T_s, Fig. 9(a). The flux correction starts taking effect in the end of $(k+1)T_s$, Fig. 9(c); the error is fully compensated at the end of $(k+3)T_s$, Fig. 9(d). In this example, only four sampling intervals elapse between the prediction of the required compensation action, Fig. 9(a), and its successful realization, Fig. 9(d). The new prediction horizon T_p is determined in Fig. 9(e).

IV. PERFORMANCE EVALUATION

The proposed MP^{3}C method was tested in the MV laboratory. The test setup consists of a MVA ACS 2000 power inverter from ABB coupled to a 6-kV, 137-A induction machine

134

TABLE I: Parameters of medium-voltage induction machine

Rated power	1.21 MW
Rated phase-to-phase voltage	6 kV rms
Rated phase current	137 A rms
Rated power factor	0.85
Rated stator frequency	50 Hz
Rated angular velocity	1488 rpm
Stator resistance	203 mΩ 0.006 p.u.
Rotor resistance	158 mΩ 0.005 p.u.
Main inductance	330 mH 2.96 p.u.
Total leakage inductance	20 mH 0.179 p.u.

TABLE II: Parameters of five-level ACS 2000 power converter

Rated apparent power	1.14 MVA
Rated phase-to-phase voltage	6.6 kV rms
DC-link voltage	9.8 kV
Rated phase current	100 A rms
Rated stator frequency	50 Hz

(a) Three-phase stator voltage waveforms and harmonic spectrum; the rms amplitude of the phase voltage is 3.49 kV.

(b) Three-phase stator current waveforms and harmonic spectrum; the rms amplitude of the phase current is 85 A. MP^{3}C produces 3.77% total demand distortion (TDD) referred to the rated current of the controlled machine (137 A).

Fig. 10: Experimental results of voltage and current waveforms produced by MP^{3}C at steady-state operation ($f_1 = 50$ Hz and 62% machine current). Optimized pulse patterns of $d = 10$ switching instants per quarter-wave are employed.

with a constant mechanical load. Important parameters of the electrical machine and of the ACS 2000 are listed in Tables I and II, respectively. The induction machine is of the direct-on-line (DOL) type, featuring very low leakage inductance. In Fig. 10, stator voltage and current waveforms are recorded in the experimental setup while the machine is operated at 50 Hz frequency and at partial load; the drive system is operated with MP^{3}C. The fundamental component of the stator voltages in Fig. 10(a) is shown only partially in the spectrum; its rms phase amplitude is 3.49 kV, which corresponds to the rated phase-to-phase machine voltage (6 kV). Higher-order voltage harmonics are shown in full detail in Fig. 10(a): discrete-order components are of negligible amplitude in the range up to the 31st harmonic.

The respective current waveforms produced by MP^{3}C are shown in Fig. 10(b): also here, the fundamental component of the current (85 A rms) is shown only partially in the spectrum. The focus of Fig. 10(b) is on the very low amplitudes of the current harmonics. MP^{3}C produces just 3.77% total demand distortion (TDD) referred to the rated current of the controlled machine (137 A). For comparison purposes, the respective voltage and current waveforms and harmonic spectra produced by direct torque control (DTC) are shown in Fig. 11. These waveforms are recorded at the same operating point and at the same switching frequency as in Fig. 10; DTC produces stator currents of 6.37% TDD.
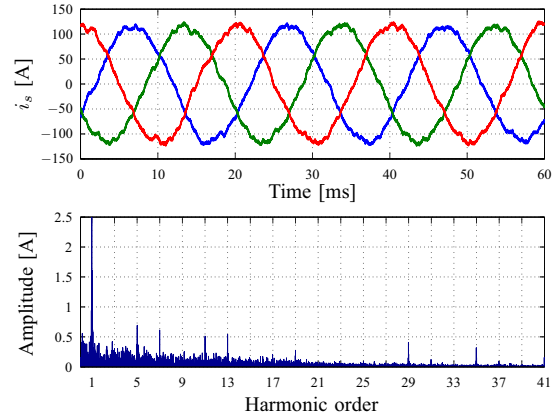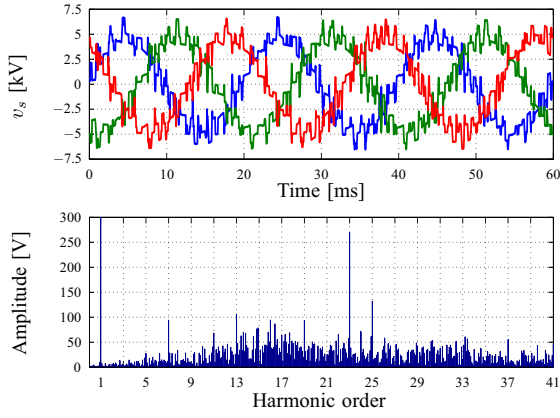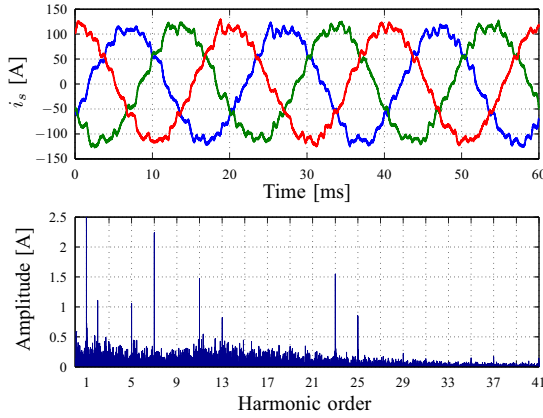
The dynamic performance of MP^{3}C was also tested in the experimental setup. A step change from full-load to no-load operation takes place at $t \approx 6.5$ ms and the recorded electromagnetic torque of the electrical machine is shown in the upper trace of Fig. 12. The fall time is kept below 4 ms with minimum undershoot. MP^{3}C achieves maintaining control of the machine even after the transient condition has elapsed, as validated by the current waveforms shown in the lower trace of Fig. 12.

V. CONCLUSIONS

Industrial medium- and high-power drives must obey stringent performance standards with regards to the total de-

mand distortion (TDD) of the currents in the windings of the controlled machine. This is a challenging task owing to the low values of switching frequency in MV setups. The solution proposed in this paper, model predictive pulse pattern control (MP^{3}C), is presented for use with the ACS 2000 five-level active neutral point clamped inverter from ABB. Optimized pulse patterns (OPPs) are calculated offline to generate minimum harmonic distortion of the currents under ideal conditions. OPPs are modified in real-time by MP^{3}C such that optimization of the stator flux trajectory is achieved. This optimization is performed in a predictive manner: required future modifications of switching instants are calculated within an event-based prediction horizon. Control actions are evaluated in a computationally effective fashion: the minimum number of required switching instants is used to compensate errors in the stator flux trajectory. This makes the application of the proposed method possible in the control

(a) Three-phase stator voltage waveforms and harmonic spectrum; the rms amplitude of the phase voltage is 3.49 kV.

(b) Three-phase stator current waveforms and harmonic spectrum; the rms amplitude of the phase current is 85 A. DTC produces 6.37% total demand distortion (TDD) referred to the rated current of the controlled machine (137 A).
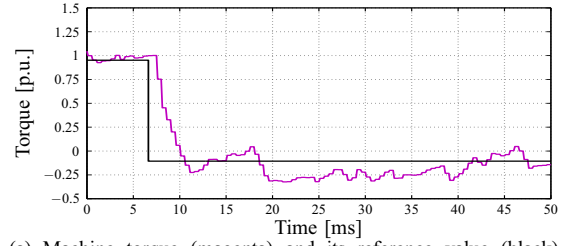
Fig. 11: Experimental results of voltage and current waveforms produced by DTC at steady-state operation ($f_1 = 50$ Hz and 62% machine current). The waveforms are recorded at the same switching frequency as in Fig. 10.
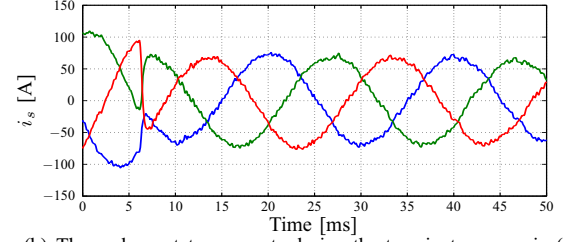
platform of any industrial drive.

MP^{3}C compensates non-idealities of the drive system that deteriorate the steady-state performance of OPPs in real-world applications. The result is minimum TDD of the produced currents even in setups that employ direct-on-line (DOL) machines, which usually feature very low leakage inductance. The superior performance of MP^{3}C was demonstrated in the laboratory with a pilot ACS 2000 MV drive operated at steady-state. The experimental setup was also subjected to a step change input of the reference torque while the drive was operated at rated frequency; the large-signal response of the electromagnetic torque of the controlled machine validates the high dynamic performance delivered by MP^{3}C.

REFERENCES

[1] F. Kieferndorf, M. Basler, L. A. Serpa, J.-H. Fabian, A. Coccia, and G. A. Scheuer, "A new medium voltage drive system based on ANPC-5L technology," in *Proc. IEEE Int. Conf. Ind. Technol.*, Via del Mar, Chile, Mar. 2010, pp. 643–649.

(a) Machine torque (magenta) and its reference value (black). The torque quantities are given in p.u..

(b) Three phase stator currents during the transient process in (a).

Fig. 12: Experimental results of a step change of the torque reference at $t \approx 6.5$ ms. The drive is operated at $f_1 = 50$ Hz.

[2] P. Barbosa, P. Steimer, J. Steinke, L. Meysenc, M. Winkelnkemper, and N. Celanovic, "Active neutral-point-clamped multilevel converters," in *Proc. IEEE Power Electron. Spec. Conf.*, Recife, Brazil, Jun. 2005, pp. 2296–2301.

[3] F. Kieferndorf, P. Karamanakos, P. Bader, N. Oikonomou, and T. Geyer, "Model predictive control of the internal voltages of a five-level active neutral point clamped converter," in *Proc. IEEE Energy Convers. Congr. Expo.*, Raleigh, North Carolina, USA, Sep. 2012.

[4] J. Holtz and N. Oikonomou, "Neutral point potential balancing algorithm at low modulation index for three-level inverter medium-voltage drives," *IEEE Trans. Ind. Appl.*, vol. 43, no. 3, pp. 761–768, May/Jun. 2007.

[5] H. S. Patel and R. G. Hoft, "Generalized techniques of harmonic elimination and voltage control in thyristor inverters: Part I—Harmonic elimination," *IEEE Trans. Ind. Appl.*, vol. IA-9, no. 3, pp. 310–317, May 1973.

[6] ——, "Generalized techniques of harmonic elimination and voltage control in thyristor inverters: Part II—Voltage control techniques," *IEEE Trans. Ind. Appl.*, vol. IA-10, no. 5, pp. 666–673, Sep. 1974.

[7] G. S. Buja and G. B. Indri, "Optimal pulsewidth modulation for feeding ac motors," *IEEE Trans. Ind. Appl.*, vol. IA-13, no. 1, pp. 38–44, Jan. 1977.

[8] J. Holtz and N. Oikonomou, "Estimation of the fundamental current in low-switching-frequency high dynamic medium voltage drives," *IEEE Trans. Ind. Appl.*, vol. 44, no. 5, pp. 1597–1605, Sep./Oct. 2008.

[9] T. Geyer, N. Oikonomou, G. Papafotiou, and F. Kieferndorf, "Model predictive pulse pattern control," *IEEE Trans. Ind. Appl.*, vol. 48, no. 2, pp. 663–676, Mar./Apr. 2012.

[10] J. B. Rawlings and D. Q. Mayne, *Model predictive control: Theory and design*.   Madison, WI, USA: Nob Hill Publ., 2009.

[11] J. M. Maciejowski, *Predictive control with constraints*.   Prentice-Hall, 2002.

[12] J. Holtz and J. Quan, "Drift and parameter compensated flux estimator for persistent zero stator frequency operation of sensorless controlled induction motors," *IEEE Trans. Ind. Appl.*, vol. 39, no. 4, pp. 1052–1060, Jul./Aug. 2003.

[13] J. Holtz, "The representation of AC machine dynamics by complex signal flow graphs," *IEEE Trans. Ind. Electron.*, vol. 42, no. 3, pp. 263–271, Jun. 1995.

[14] D. Luenberger, "An introduction to observers," *IEEE Trans. Automat. Contr.*, vol. 16, no. 6, pp. 596–602, Dec. 1971.